drones

Article

Robust Position Control of VTOL UAVs Using a Linear Quadratic Rate-Varying Integral Tracker: Design and Validation

Omer Saleem [1], Muhammad Kazim [2] and Jamshed Iqbal [3,*]

[1] Department of Electrical Engineering, National University of Computer and Emerging Sciences, Lahore 54770, Pakistan
[2] Center for Robotics and Autonomous Systems, Khalifa University, Abu Dhabi 127788, United Arab Emirates
[3] School of Computer Science, Faculty of Science and Engineering, University of Hull, Hull HU6 7RX, UK
* Correspondence: j.iqbal@hull.ac.uk

Abstract: This article presents an optimal tracking controller retrofitted with a nonlinear adaptive integral compensator, specifically designed to ensure robust and accurate positioning of Vertical Take-Off and Landing (VTOL) Unmanned Aerial Vehicles (UAVs) that utilize contra-rotating motorized propellers for differential thrust generation. The baseline position controller is synthesized by employing a fixed-gain Linear Quadratic Integral (LQI) tracking controller that stabilizes position by tracking both state variations and pitch-axis tracking error integral, which adjusts the voltage to control each coaxial propeller's speed accurately. Additionally, the baseline tracking control law is supplemented with a rate-varying integral compensator. It operates as a nonlinear scaling function of the tracking-error velocity and the braking acceleration to enhance the accuracy of reference tracking without sacrificing its robustness against exogenous disruptions. The controller's performance is analyzed by performing experiments on a tailored hardware-in-the-loop aero-pendulum testbed, which is representative of VTOL UAV dynamics. Experimental results demonstrate significant improvements over the nominal LQI tracking controller, achieving 17.9%, 61.6%, 83.4%, 43.7%, 35.8%, and 6.8% enhancement in root mean squared error, settling time, overshoot during start-up, overshoot under impulsive disturbance, disturbance recovery time, and control energy expenditure, respectively, underscoring the controller's effectiveness for potential UAV and drone applications under exogenous disturbances.

Keywords: VTOL UAVs; position tracking; linear quadratic integral control; rate-varying integral compensator; hyperbolic function; hardware-in-the-loop validation

Academic Editor: Abdessattar Abdelkefi

Received: 9 December 2024
Revised: 11 January 2025
Accepted: 16 January 2025
Published: 19 January 2025

Citation: Saleem, O.; Kazim, M.; Iqbal, J. Robust Position Control of VTOL UAVs Using a Linear Quadratic Rate-Varying Integral Tracker: Design and Validation. *Drones* **2025**, *9*, 73. https://doi.org/10.3390/drones9010073

1. Introduction

The Vertical Take-Off and Landing (VTOL) Unmanned Aerial Vehicle (UAV) is a flight dynamic system that is utilized in various aerospace applications because of its versatility and ability to hover, take off, and land vertically [1,2]. Their lack of dependence on a dedicated runway provides them with the necessary operational flexibility. Some of the key applications of VTOL UAVs include aerial videography, surveillance for security, search and rescue, precision agriculture to optimize farming practices, environmental and infrastructure inspection, and package delivery [3,4]. The aerodynamically driven pendulum systems imitate the flight dynamics of a VTOL rotorcraft. They are thus preferred as ideal candidates to validate the VTOL control strategies in a laboratory environment [5]. The aero-pendulum comprises an apparatus rod with a motorized propellor at one end to generate the thrust for take-off while the other end is pivoted about a rotational encoder to measure the system's pitch angle [6]. The motorized propeller attached to the rod's tail generates the thrust that is dynamically adjusted to regulate the rotorcraft's pitch. The tail elevator also aids in continuously reorienting the VTOL UAV while tracking time-varying reference trajectories or compensating for external perturbations during the flight mode [7].

The utilization of the coaxial rotor assembly has garnered a lot of attention in recent VTOL UAV system designs [8]. Where two motorized propellers are commissioned on the rod's tail such that one rotates in the opposite direction to the other [9]. Consequently, both propellers generate torques that are equal in magnitude but act in opposite directions, canceling each other out. The differential thrust thus generated by the contra-rotating propellers effectively eliminates the heeling moment caused by the torque created in a single propeller system [10]. This arrangement can continue to self-stabilize the system in the event of a motor failure, making it far less likely to cause an accident.

1.1. Related Work

Owing to their under-actuated configuration, the VTOL aero-pendulum systems require agile control efforts to regulate their posture during take-off and landing and to track reference trajectories during flight [11]. This control problem becomes significantly harder when the system encounters exogenous disturbances, parametric uncertainties, severe weather patterns, or abrupt load changes [12]. Numerous VTOL control methodologies are suggested in the scientific literature to deal with such circumstances [13,14]. The pervasive Proportional–Integral–Derivative (PID) controllers are well known for their reliable control yield; however, their design simplicity limits their performance against exogenous disturbances [15]. Without auxiliary augmentations, they lack the flexibility to effectively address the VTOL's intrinsic nonlinear dynamics [6]. As compared to conventional PID controllers, the Fractional Order PID (FOPID) controller design provides increased versatility by incorporating fractional derivative and integral operators, which improves the system's robustness against random disturbances and environmental indeterminacies [16]. However, optimizing the FOPID controllers is more complex and computationally intensive due to the fractional parameters [17]. The model predictive controllers can effectively handle the constraints posed by the complex dynamics of the VTOL systems; however, their high real-time processing requirements make them computationally intensive [18].

The fuzzy logic controllers offer an intuitive design, and their behavior can be customized by reconfiguring the linguistic rules and the associated membership functions, which supplements the controller's adaptability [19]. However, the fine-tuning of the rules and membership functions is a labor-intensive task that requires expert knowledge [20]. The neural network-based controllers can self-learn the dynamics of the VTOL aero-pendulum and self-tune the critical controller parameters via training, providing optimum control decisions as the operating conditions vary [21]. The training process autonomously designs the compensator, which does not necessitate manual parameter tuning. However, neural controller synthesis requires large sets of training data, which makes it computationally expensive [22]. The RL controllers do not require an accurate mathematical model of the aero-pendulum. Instead, they can learn and adapt to state variations through continuous interaction with the environment, making them suitable for aero-dynamics systems [23]. However, this technique has a data-intensive nature and may lead to unsafe actions during the learning phase.

Nonlinear controllers are formulated to address the intrinsic nonlinearities of aerodynamic systems, offering enhanced robustness across a broader range of operating conditions, which reduces the need for linearization [24,25]. However, they typically require a detailed and accurate mathematical model, which can be challenging to derive [26]. Additionally, the model derivation and identification via complex mathematical tools tends to increase the algorithm's computational burden [27]. The backstepping control is renowned for its good tracking performance [28]. However, they have a complex design that requires extensive tuning and are highly sensitive to measurement noise [29]. The Sliding Mode Control scheme is extensively utilized to robustly reject the perturbations and uncertainties in nonlinear systems; however, the high-frequency switching induces chattering in the control signal, which affects the actuator's health [30].

The Linear Quadratic Regulator (LQR) is highly favored for optimal control of underactuated mechatronic systems by taking into account the state dynamics and control profile of a linearized VTOL system [31]. However, its dependence on the dynamics of VTOL UAVs limits its resilience against the unmodeled nonlinear characteristics and, thus, renders it sensitive to external perturbations and modeling inaccuracies [32]. Additionally, the nominal LQR structure is also ineffective in tracking control applications [33]. Generally, an integrator operating on the state error in pitch angle (connected in unity feedback) is introduced in the LQR law for asymptotic tracking of time-varying reference positions [34]. The linear quadratic integral (LQI) trackers offer faster and smoother transient responses by leveraging full-state feedback, which naturally addresses these couplings. Dynamic output controllers, while theoretically capable, often involve intricate tuning procedures that increase design complexity, especially for nonlinear or time-varying systems like VTOL [35]. Output-based controllers, particularly static ones, rely on a subset of output states and may struggle to handle inter-variable dependencies efficiently [36]. They exhibit limited control authority over unmeasured dynamics, which can degrade transient performance. Despite the efficacy of the LQI trackers, concurrently achieving accurate reference tracking and robust disturbance rejection in VTOL UAVs during flight mode is a challenge for scientists.

Finally, handling actuator saturation is a critical factor in controlling VTOL systems. The study in [37] presents a delay-kernel-dependent approach to improve control performance under actuator saturation and mixed delays, guaranteeing better system stabilization. Similarly, the study in [38] uses interval type-2 fuzzy logic to provide a distributed-delay-dependent framework for stabilizing systems with stochastic delays as well as actuator saturation. Despite their efficacies, the methodologies discussed above are not well-suited to address the complex coupling issues associated with the VTOL systems.

1.2. Salient Contributions

The salient contribution of this article is to devise an optimal position-tracking controller retrofitted with a nonlinear adaptive integral compensator that ensures robust tracking simultaneous with strong disturbance rejection in VTOL systems. The ubiquitous LQI compensator is used as the baseline tracking controller for the aero-pendulum-type VTOL systems with coaxial contra-rotating propellers. The asymptotic stability analysis of the baseline LQI tracking controller is also discussed subsequently. The prescribed control scheme is realized by replacing the integral portion of the LQI tracker with a nonlinear rate-varying integral (RVI) compensator instead, which enhances the system's reference-tracking accuracy as well as its adaptability against exogenous perturbations. This article's innovative contributions are postulated below:

1. Augmenting the integral portion in the baseline LQI tracking control law with an RVI compensator to further robustify the controller's performance. A nonlinear hyperbolic function of the system's tracking-error velocity as well as its braking acceleration is used to formulate the RVI compensator.

2. Verification of the proposed compensator design by conducting hardware-in-the-loop (HIL) experiments on a custom-designed laboratory-scale aero-pendulum platform with contra-rotating propellers.

The proposed modifications yield a robust and accurate position controller that offers excellent tracking and disturbance rejection capabilities. Owing to its adaptability, the proposed controller efficiently responds to both small and large variations in the reference positions despite the VTOL system's many inherent nonidealities. Finally, the RVI compensator enables the tracking control law to quickly revert the direction of the state response without contributing large oscillations and overshoots (or undershoots). The proposed enhancements to the LQI compensator are specifically tailored for robust tracking and disturbance rejection in VTOL UAV systems.

In contrast to the adaptive controller design proposed in [6] that relies on 49 pre-calibrated fuzzy rules for online adaptation of a single parameter, the proposed approach employs a hyperbolic scaling function that dynamically adapts the integral term in the control law to tracking error velocity and braking acceleration to provide a more flexible and robust control effort. In comparison to the fuzzy-adaptive control law, this scheme is computationally economical. Additionally, the RVI's incorporation into the compensator design increases the controller's design flexibility, which helps reduce oscillations and overshoots more efficiently than the fuzzy-adaptive PID framework suggested in [6], underscoring the enhanced transient performance and adaptability of the proposed scheme.

The design and validation of an LQI tracking controller with an RVI compensator for accurate positioning and robust tracking control of an aero-pendulum-based VTOL system has not been attempted in the scientific literature available. Hence, this article explores this innovative idea.

The remainder of the paper is organized into five sections: The system's mathematical model and the baseline state space tracking controller are derived in Section 2. The control law is formulated in Section 3. The offline parameter-tuning procedure is discussed in Section 4. The comparative analysis of the designed controllers via customized hardware experiments is performed in Section 5. Finally, Section 6 concludes the paper.

2. System Modeling and Control

The derivation of the aero-pendulum's state space model, as well as the constitution of its closed-loop optimal tracking control scheme, is presented in the following section. The schematic representing the aero-pendulum's free-body diagram is illustrated in Figure 1 [6]. The aero-pendulum system considered in this work comprises two coaxial motorized propellers commissioned on the tail of the pendulum's rod, as shown in Figure 2 [39].

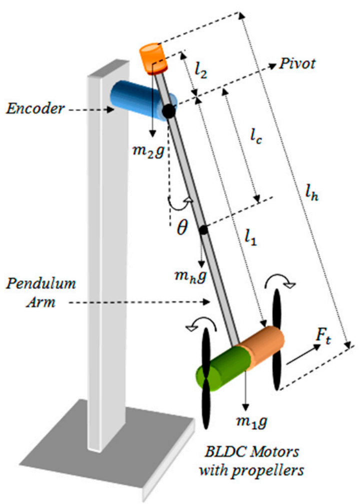

Figure 1. Free-body diagram of the aero-pendulum positioning system [6].

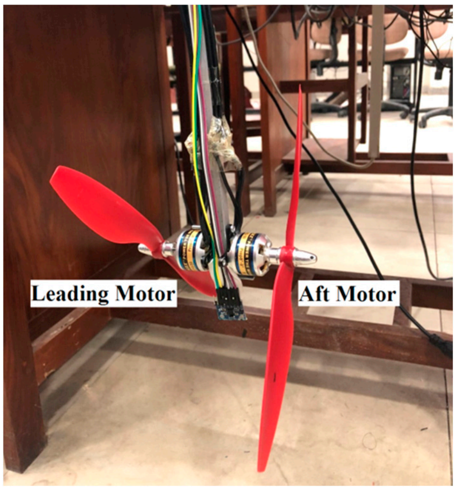

Figure 2. Coaxial motors with propellers [6].

2.1. Aero-Pendulum Modeling

The derivation of the transfer function and its state-space model of the aero-pendulum-type VTOL system is presented below [39]. Equation (1) describes the torques operating on the rigid body system:

$$\tau_t - m_1 g \cos\big(\theta(t)\big)\, l_1 + m_2 g \cos\big(\theta(t)\big)\, l_2 - \frac{1}{2} m_h g \cos\big(\theta(t)\big)\, l_h = 0 \tag{1}$$

where τ_t is the torque acting on the pendulum, m_1 is the pendulum arm's mass, g is the acceleration due to gravity, θ is the pendulum's angular position with respect to the vertical axis (as shown in Figure 1), l_1 is the distance between the propellers and the pivot point, m_2 is the pendulum's counter mass, l_2 is the distance between the counter mass and the pivot point, m_h is the pendulum's total mass, and l_h is the pendulum arm's total length. The propeller generates a thrust force (F_t), which acts perpendicular to the rotor assembly. The resultant torque (τ_t) is given by Equation (2) [40]

$$\tau_t = F_t l_1 = K_t I_m(t) \tag{2}$$

where K_t is the current-torque constant and I_m represents the motor's current. The propeller's torque, as well as the counter mass's gravitational torque, act in the same direction, reinforcing one another. The thrust is continually varied until the pendulum stabilizes at the desired reference position. The torque applied to the system at equilibrium is determined by Equation (3) [40]:

$$K_t I_m(t) - m_1 g l_1 + m_2 g l_2 - \frac{1}{2} m_h g l_h = 0 \tag{3}$$

The second-order differential equation describing the pendulum's rotational motion in relation to the thrust torque is given by Equation (4) [41]:

$$J\ddot{\theta}(t) + B\dot{\theta}(t) + K\theta(t) = K_t I_m(t) \tag{4}$$

where J, B, and K represent the pendulum's moment of inertia along the pitch axis, its viscous-damping coefficient, and its stiffness coefficient, respectively. A composite body's moment of inertia with q point-masses is given by Equation (5):

$$J = \sum_{k=1}^{q} m_k r_k^2 \tag{5}$$

where m_k represents the body's mass and r_k represents the distance between the k^{th} object and the axis of rotation. The transfer characteristics relating to the pendulum's angular position with its motor's input current are expressed in Equation (6):

$$\frac{\theta(s)}{I_m(s)} = \frac{\frac{K_t}{J}}{s^2 + \frac{B}{J}s + \frac{K}{J}} \tag{6}$$

The differential equation governing the motor dynamics is presented as follows [37]:

$$L_m \dot{I}_m(t) + R_m I_m(t) = V_m(t) \tag{7}$$

where L_m is the motor's internal inductance, R_m is the motor's resistance, and V_m is the motor's control input voltage. The transfer function of the DC motor is presented as shown in Equation (8):

$$\frac{I_m(s)}{V_m(s)} = \frac{\frac{1}{L_m}}{s + \frac{R_m}{L_m}} \tag{8}$$

By combining Equations (6) and (8), the system's transfer function is presented as shown below:

$$\frac{\theta(s)}{V_m(s)} = \frac{b}{s^3 + a_1 s^2 + a_2 s + a_3} \tag{9}$$

where $a_1 = \frac{B}{J} + \frac{R_m}{L_m}, a_2 = \frac{K}{J} + \frac{BR_m}{JL_m}, a_3 = \frac{KR_m}{JL_m}, b = \frac{K_t}{JL_m}$

Table 1 describes the aforementioned modeling parameters. The expression in Equation (6) is transformed into the time domain, as shown in Equation (10).

$$\dddot{\theta}(t) + a_1\ddot{\theta}(t) + a_2\dot{\theta}(t) + a_3\theta(t) = bV_m(t) \tag{10}$$

As discussed earlier, the baseline control law is augmented with an auxiliary position error integral variable $\varepsilon(t)$, expressed in Equation (11), to optimize the reference-tracking accuracy and robustness against bounded perturbations [42]:

$$\varepsilon(t) = \int e(t)\, dt \tag{11}$$

such that, $e(t) = \theta_{ref}(t) - \theta(t)$.

Where $e(t)$ computes the error between the system's actual position $\theta(t)$ and reference position $r(t)$. The differential equations formulated above are used to derive the state-space model of the system. Equation (12) represents the mathematical form of a linear system:

$$\dot{x}(t) = \boldsymbol{A}x(t) + \boldsymbol{B}u(t) + \boldsymbol{F}r(t), y(t) = \boldsymbol{C}x(t) + \boldsymbol{D}u(t) \tag{12}$$

where $x(t)$, $y(t)$, $u(t)$, and $r(t)$ are the system's sate vector, output vector, control input, and the reference position input, respectively. The matrices $\boldsymbol{A}$, $\boldsymbol{B}$, $\boldsymbol{F}$, $\boldsymbol{C}$, and $\boldsymbol{D}$ denote the system matrix, control input matrix, reference input matrix, output matrix, and feed-forward matrix, respectively. The system's state vector as well as its control input vector are identified in Equation (13).

$$x(t) = [\theta(t) \quad \dot{\theta}(t) \quad \ddot{\theta}(t) \quad \varepsilon(t)]^T, u(t) = V_m(t) \tag{13}$$

The aero-pendulum VTOL system's state-space model is expressed in Equation (14) [10].

$$\boldsymbol{A} = \begin{bmatrix} 0 & 1 & 0 & 0 \\ 0 & 0 & 1 & 0 \\ -a_3 & -a_2 & -a_1 & 0 \\ -1 & 0 & 0 & 0 \end{bmatrix}, \boldsymbol{B} = \begin{bmatrix} 0 \\ 0 \\ b \\ 0 \end{bmatrix}, \boldsymbol{F} = \begin{bmatrix} 0 \\ 0 \\ 0 \\ 1 \end{bmatrix}, \boldsymbol{C} = \begin{bmatrix} 1 & 0 & 0 & 0 \\ 0 & 1 & 0 & 0 \\ 0 & 0 & 1 & 0 \\ 0 & 0 & 0 & 1 \end{bmatrix}, \boldsymbol{D} = \begin{bmatrix} 0 \\ 0 \\ 0 \\ 0 \end{bmatrix} \quad (14)$$

The position variables $\theta(t)$, $\dot{\theta}(t)$, $\ddot{\theta}(t)$, and the error-integral variable $\varepsilon(t)$ are the output variables of the system. The model parameters of the aero-pendulum testbed used in this research work are given in Table 1 [16].

Table 1. Model parameters of the experimental aero-pendulum setup [6].

Parameters	Description	Value	Units
K_t	Current-torque constant	0.029	Nm/V
J	Moment of inertia	0.058	kgm^2
B	Viscous-damping coefficient	0.041	Nms/rad
K	Stiffness coefficient	0.320	kgm^2/s^2
R_m	Motor resistance	3.0	Ω
L_m	Motor inductance	0.06	H

2.2. Baseline LQI Tracker Formulation

This section formulates the baseline LQI tracker for the accurate position of the aero-pendulum VTOL system. The LQI tracker is a full-state feedback tracking control procedure that optimizes the system's reference-tracking accuracy and effectively dampens the overshoots (and undershoots) by retrofitting the conventional LQR law with an error-integral state variable [43]. The first step is to minimize a Quadratic Performance Index (QPI), expressed in Equation (15), of the control input and state variables [44].

$$J_{lq} = \frac{1}{2}\int_0^{\infty} (x(t)^T \boldsymbol{Q} x(t) + u(t)^T \boldsymbol{R} u(t))\, dt \quad (15)$$

where $\boldsymbol{Q} \in \mathbb{R}^{4\times4}$ is a preset positive semi-definite state-weighting matrix and $\boldsymbol{R} \in \mathbb{R}$ is a preset positive definite control-weighting matrix. The aforementioned weighting matrices penalize the changes in the control input and the states. The $\boldsymbol{Q}$ and $\boldsymbol{R}$ matrices used for the proposed VTOL system are represented as shown in Equation (16).

$$\boldsymbol{Q} = \mathrm{diag}(q_\theta \quad q_{\dot{\theta}} \quad q_{\ddot{\theta}} \quad q_\varepsilon), \boldsymbol{R} = p \quad (16)$$

The coefficients of these matrices are selected such that $q_x \geq 0$ and $p > 0$. This condition is a necessary requirement to yield an asymptotically stable control law. The offline tuning procedure used to optimize these coefficients is discussed in Section 4. Once the aforementioned weighting matrices are optimized offline, the Hamilton–Jacobi–Bellman (HJB) equations are used to derive the optimal tracking control law. Their solution delivers the Algebraic Riccati Equation (ARE) given in Equation (17) [44]:

$$\boldsymbol{A}^T\boldsymbol{P} + \boldsymbol{P}\boldsymbol{A} - \boldsymbol{P}\boldsymbol{B}\boldsymbol{R}^{-1}\boldsymbol{B}^T\boldsymbol{P} + \boldsymbol{Q} = 0 \quad (17)$$

where $\boldsymbol{P} \in \mathbb{R}^{4\times4}$ is the solution of the ARE. It is a positive definite symmetric matrix. The optimal gain vector $\boldsymbol{K}$ is evaluated as mentioned in Equation (18) [44]:

$$\boldsymbol{K} = \boldsymbol{R}^{-1}\boldsymbol{B}^T\boldsymbol{P} \quad (18)$$

where $\boldsymbol{K} = [k_\theta \quad k_{\dot{\theta}} \quad k_{\ddot{\theta}} \quad k_\varepsilon]$. The nominal LQI control law is indicated in Equation (19).

$$u(t) = -\boldsymbol{K}x(t) \quad (19)$$

The LQI tracker's asymptotic convergence is investigated via the following Lyapunov function [17]:

$$Z(t) = x(t)^T\boldsymbol{P}x(t) > 0, \text{for } x(t) \neq 0 \quad (20)$$

Stability Proof*:* The first derivative of $Z(t)$ is derived, as shown below.

$$\begin{aligned}\dot{Z}(t) &= 2x(t)^T\boldsymbol{P}\dot{x}(t)\\ &= 2x(t)^T\boldsymbol{P}(\boldsymbol{A}-\boldsymbol{BK})x(t)\\ &= 2x(t)^T\boldsymbol{P}(\boldsymbol{A}-\boldsymbol{BR}^{-1}\boldsymbol{B}^T\boldsymbol{P})x(t)\\ &= x(t)^T(\boldsymbol{PA}+\boldsymbol{A}^T\boldsymbol{P})x(t) - 2x(t)^T(\boldsymbol{PBR}^{-1}\boldsymbol{B}^T\boldsymbol{P})x(t)\end{aligned} \tag{21}$$

By substituting Equation (17) in Equation (21), $\dot{Z}(t)$ is simplified as shown below.

$$\dot{Z}(t) = -x(t)^T\boldsymbol{Q}x(t) - x(t)^T(\boldsymbol{PBR}^{-1}\boldsymbol{B}^T\boldsymbol{P})x(t) < 0 \tag{22}$$

Hence, if $\boldsymbol{R} = \boldsymbol{R}^T > 0$ and $\boldsymbol{Q} = \boldsymbol{Q}^T \geq 0$, then $\dot{Z}(t)$ is a negative-definite function. Thus, satisfying the above conditions can preserve the asymptotic stability of the designed LQI tracker.

Figure 3 shows the block diagram of the LQI control approach. The voltage control signals provided by the LQI tracker are applied to the leading and the aft motors. To realize the contra-rotating motion, the same magnitudes but opposite polarities of the voltage signals are applied to the leading and the aft motors, as shown in Figure 3. This arrangement aids in nullifying the heeling moment generated otherwise. The actuators use the applied input voltage to produce appropriate current signals that rotate the motorized propellers, which eventually helps the aero-pendulum to track the reference position.

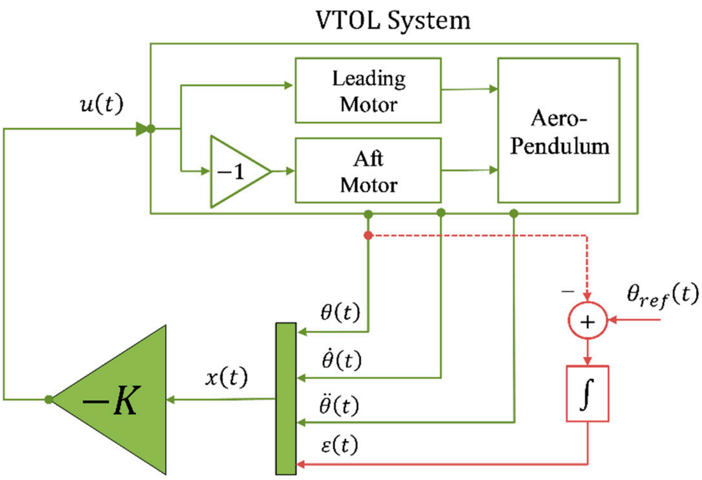

Figure 3. Block diagram of the baseline LQI tracking control scheme. Red lines indicate the add-on to the conventional control scheme to highlight the novelty of the present work.

3. Proposed Control Methodology

This section documents the systematic formulation of a nonlinear LQI tracker to deliver robust tracking and disturbance rejection while addressing the nonidealities that exist in the aero-pendulum system, such as integrator wind-up, stiction, and overshoots caused by the rapid variations in the setpoint [45].

The proposed control scheme's design strategy is discussed below. Consider the baseline LQI tracking control law expressed in Equation (19).

The baseline control law $u(t) = -\boldsymbol{K}x(t)$ is expanded and rewritten as expressed in the following equation:

$$u(t) = -\boldsymbol{K_\theta}x_\theta(t) - k_\varepsilon\varepsilon(t) \tag{23}$$

where $\boldsymbol{K_\theta} = [k_\theta \quad k_{\dot{\theta}} \quad k_{\ddot{\theta}}]$ and $x_\theta(t) = [\theta(t) \quad \dot{\theta}(t) \quad \ddot{\theta}(t)]^T$. From Equation (11), the following expression can be deduced:

$$\dot{\varepsilon}(t) = e(t) \tag{24}$$

By using numerical differentiation,

$$\frac{\varepsilon(t)-\varepsilon(t-T)}{T}=e(t) \tag{25}$$

where T is the sampling interval. The above expression can also be written as the following:

$$\varepsilon(t)=\varepsilon(t-T)+e(t)\,T \tag{26}$$

The RVI scheme is realized by retrofitting the error-integral $\varepsilon(t)$, expressed in Equation (26), with the following two auxiliary nonlinear adaptation blocks [45]:

1. Velocity-driven integral modulator: To deal with the nonidealities (integral wind-up and stiction problems) inherent to the aero-pendulum system.
2. Braking-acceleration compensator: To dampen the transient disturbances and overshoots while maintaining the tracking speed and accuracy of the aero-pendulum as per the changes in the braking acceleration of the reference trajectory.

The augmentation of the pre-calibrated nonlinear adaptation blocks tends to increase the proposed control law's adaptability and responsivity to nonlinear dynamics and exogenous disturbances while preserving the system's control economy for a broad range of reference trajectories (multi-step, ramp, and sinusoidal). The following sub-sections present a step-by-step development of the aforementioned nonlinear adaptation blocks and their augmentation with the proposed control law.

3.1. Velocity-Driven Integral Modulator

The nominal LQI controller typically lacks robustness against step changes in the reference positions and, thus, inevitably exhibits large overshoots (or undershoots) due to the actuator saturation caused by the integral wind-up [45]. Additionally, the effects of stiction at the mechanical joint, as well as the actuator deadband, unavoidably lead to a delay in the tracking response for the ramp and sinusoidal reference trajectories. The large overshoots associated with the integral wind-up are most prominent under large step changes when the system is required to track and approach the new setpoint quickly, despite the large step change. Hence, the occurrence of the overshoots is driven by the system's velocity $\dot{\theta}(t)$. The error velocity of the aero-pendulum is expressed as follows:

$$\dot{e}(t)=\dot{\theta}_{ref}(t)-\dot{\theta}(t) \tag{27}$$

For step changes in the reference, the variations in $\dot{e}(t)$ are proportional to the variations in the system's velocity $\dot{\theta}(t)$. The aforementioned problem is thus addressed by augmenting the LQI tracker's error-integral variable $\varepsilon(t)$ with a bounded and even-symmetric nonlinear function driven by the system's velocity error $\dot{e}(t)$. The nonlinear function is designed via the following metarules [45]:

1. The magnitude of the nonlinear factor is kept high (closer to unity) when $\dot{e}(t)$ is low, which maintains the integral term in its normal form and allows it to yield nominal control action.
2. The magnitude of the nonlinear factor is gradually made smaller (closer to zero) when $\dot{e}(t)$ increases, which reduces the impact of the integral term and softens the integral control yield.

This nonlinear factor iteratively multiplies with the entire cumulative integral, causing the integral to reset itself at high velocities (when the set point is changing abruptly) and minimizing overshoot caused by the integral windup. As per the aforementioned metarules, a bounded and even-symmetric nonlinear algebraic function of the system's velocity error $\dot{e}(t)$ is required to formulate the nonlinear factor. Hence, a velocity error-driven hyperbolic secant function (HSF) is used in this research. The expression of the proposed error velocity-driven integral modulator (VDIM), constituted to attenuate the overshoots due to integral wind-up, is shown in Equation (28):

$$\varepsilon(t) = (\varepsilon(t - T) + e(t)\,T)\,m(t) \tag{28}$$

such that $m(t) = \mathrm{sech}\big(\alpha\,\dot{e}^2(t)\big)$ where $\mathrm{sech}(.)$ denotes the HSF, and α represents the HSF's variation rate. The static friction inhibits the aero-pendulum's reference tracking. Due to friction, the pendulum's velocity $\dot{\theta}(t)$ becomes negligible while the magnitude of velocity error $\dot{e}(t)$ enlarges. This phenomenon inevitably reduces the magnitude of the nonlinear factor, $m(t)$, which in turn yields a reasonably softer integral control action. This arrangement renders the nonlinear factor ineffective and leads to large overshoots. The waveform of the VDIM is shown in Figure 4.

The variance of the nonlinear factor depends on α. A small-fixed setting of α renders the $m(t)$ less responsive to $\dot{e}(t)$ variations, degrading the system's setpoint tracking capability. Conversely, a large-fixed setting of α makes $m(t)$ highly responsive to the abrupt variations in $\dot{e}(t)$, but it also makes the control input highly discontinuous and inevitably introduces oscillations in the state response as $\dot{e}(t)$ oscillates between the regions of high- and low-velocity errors. To address this issue, the variation rate α is adaptively modulated online via a pre-calibrated regulator that is driven by the variations in the reference velocity $\dot{\theta}_{ref}$, as shown in Equation (29).

$$\alpha(t) = \alpha_{\max}\left(0.01 + \mathrm{sech}\left(\frac{\left|\dot{\theta}_{ref}\right|}{\dot{\theta}_{\max}}\right)\right) \tag{29}$$

The value of $\alpha_{\max}$ is calibrated offline by using the parameter selection procedure presented in Section 4. This arrangement is very beneficial as it reduces α under large $\dot{e}(t)$ caused by stiction.

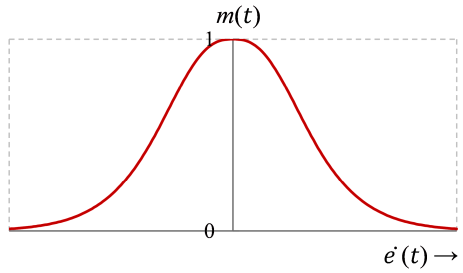

Figure 4. Waveform of the VDIM.

The small α slows down the variation rate of $m(t)$ causing it to expand. This maintains $m(t)$ at a relatively larger magnitude, which aids in applying a tighter control effort to address the stiction. Conversely, under small $\dot{e}(t)$ or non-stiction, the value of α is inflated to speed up the variation rate of $m(t)$, making the integral control term regain its robustness and adaptability to changes in $\dot{e}(t)$. With this implantation of the said augmentation, the modified expression of the error VDIM is expressed as shown in Equation (30).

$$\varepsilon(t) = (\varepsilon(t - T) + e(t)\,T)\;\mathrm{sech}\big(\alpha(t)\,\dot{e}^2(t)\big) \tag{30}$$

3.2. Braking–Acceleration Compensator

The LQI controller is utilized to track reference trajectories accurately while effectively minimizing tracking errors. Despite its ability to accurately track the setpoint at constant velocities, the integral term itself changes slowly. However, in the reference trajectories with abruptly changing velocities, the sluggish integral behavior typically leads to ineffective setpoint tracking [45]. This phenomenon inevitably results in large overshoots, particularly at corner points of the reference trajectory where the velocity setpoint sharply transits to zero. Even with the augmentation of the prescribed VDIM, the integral term sluggishly reduces to zero at the resting point (zero setpoint velocity) of the reference trajectory. To attenuate the overshoots during the braking phase, a braking-acceleration compensator (BAC) is introduced alongside the tracking error in the modified integrator expression, as shown below.

$$\varepsilon(t) = \left(\varepsilon(t-T) + \left(e(t) + K_a\,\ddot{\theta}_{braking}\right)T\right)\,\mathrm{sech}\left(\alpha(t)\,\dot{e}^2(t)\right) \tag{31}$$

where $\ddot{\theta}_{braking}$ is the braking acceleration and K_a is the pre-defined weightage associated with it. The weighted braking acceleration term nullifies the impact or error in calculating the integral term. Consequently, this modification enables the integral to die down quickly when the velocity setpoint approaches zero, which effectively prevents the occurrence of large overshoots.

It is to be noted that a system enters its braking phase when its relative rate is negative. The relative rate informs the system regarding the dynamic speed (acceleration or deceleration) of the reference trajectory. The relative rate of the reference trajectory is computed as the product of its velocity $\dot{\theta}_{ref}$ and acceleration $\ddot{\theta}_{ref}$, at a given instant, as shown below [45]:

$$q(t) = \ddot{\theta}_{ref}\dot{\theta}_{ref} \tag{32}$$

The braking acceleration depends on $\ddot{\theta}_{ref}$ of the trajectory. However, it is only activated in the RVI expression when the reference trajectory is decelerating to zero setpoint velocity (that is, $q(t) < 0$). This rule is mathematically expressed as follows [45].

$$\ddot{\theta}_{braking} = \begin{cases} \ddot{\theta}_{ref}\ if\ q(t) < 0 \\ 0\ if\ q(t) \geq 0 \end{cases} \tag{33}$$

To comply with the metarules discussed above, the instantaneous value of the braking acceleration is dynamically adjusted online using the following nonlinear function:

$$\ddot{\theta}_{braking} = \ddot{\theta}_{ref}\,\tanh^2\left(\delta(t)\,q(t)\right)\,\mathrm{step}\left(-q(t)\right) \tag{34}$$

where $\delta(t)$ is the time-varying variance of the even symmetric $\tanh^2(.)$ function, which represents the square of the hyperbolic-tangent function $\tanh(.)$. The $\mathrm{step}\left(-q(t)\right)$ function is unity for $q(t) < 0$, and zero otherwise. The waveform of $\ddot{\theta}_{braking}$ is shown in Figure 5. The variance of the $\tanh^2(.)$ function is adjusted inversely with respect to the variations in the magnitude of $\ddot{\theta}_{ref}$, by using the even symmetric $\mathrm{sech}(.)$ function formulation below.

$$\delta(t) = \delta_{\max}\left(0.01 + \mathrm{sech}\left(\frac{\left|\ddot{\theta}_{ref}\right|}{\ddot{\theta}_{\max}}\right)\right) \tag{35}$$

The value of $\delta_{\max}$ is calibrated offline by using the parameter selection procedure presented in Section 4. The time-varying variance $\delta(t)$ offers several merits in regulating the braking acceleration.

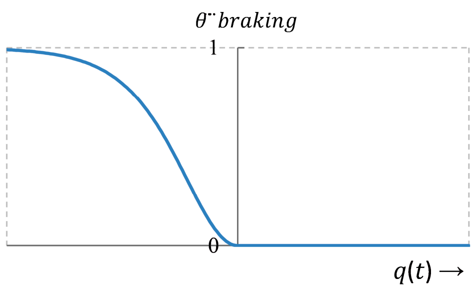

Figure 5. Waveform of the braking–acceleration compensator.

Firstly, it enables smooth modulation of the acceleration, avoiding abrupt changes that could introduce instability or cause jerky movements caused by rapid trajectory shifts. Secondly, it allows the controller to adapt to dynamic conditions, such as changes in payload or joint friction, which ensures robust performance across various operating scenarios. Thirdly, it dynamically adjusts the sensitivity of the function, dictating the $\ddot{\theta}_{braking}$ in proportion to the magnitude of $q(t)$, allowing precise error correction for effective trajectory tracking. Finally, this approach prevents over-correction by flattening the response when deviations are small while ensuring faster corrections for larger errors to maintain stability. Additionally, by matching the braking effort to the required level, the control energy consumption is minimized, which eventually optimizes the performance of robotic systems—especially those powered by batteries.

3.3. Proposed Control Law Formulation

As discussed earlier, the RVI scheme is synthesized by augmenting the integrator term of the LQI with the VDIM and BAC functions, respectively. The LQI controller, thus retrofitted with a pre-configured adaptive nonlinear RVI, is referred to as the LQ-RVI controller in this study. The proposed LQ-RVI control law is expressed in Equation (36).

$$u(t) = -\boldsymbol{K_\theta} x_\theta(t) - k_\varepsilon \varepsilon(t) \tag{36}$$

The RVI variable $\varepsilon(t)$ is dynamically adjusted after every sampling interval, as shown below:

$$\varepsilon(t) = \left(\varepsilon(t-T) + \left(e(t) + K_a\, \ddot{\theta}_{braking}\right) T\right) \operatorname{sech}\left(\alpha(t)\, \dot{e}^2(t)\right) \tag{37}$$

such that, $\ddot{\theta}_{braking} = \ddot{\theta}_{ref} \tanh^2\left(\delta(t)\, q(t)\right) \operatorname{step}\left(-q(t)\right)$,

where $q(t) = \ddot{\theta}_{ref}\dot{\theta}_{ref}, \delta(t) = \delta_{\max}\left(0.01 + \operatorname{sech}\left(\frac{|\ddot{\theta}_{ref}|}{\ddot{\theta}_{\max}}\right)\right)$,

and, $\alpha(t) = \alpha_{\max}\left(0.01 + \operatorname{sech}\left(\frac{|\dot{\theta}_{ref}|}{\dot{\theta}_{\max}}\right)\right)$.

The LQ-RVI tracking controller's block diagram is depicted in Figure 6.

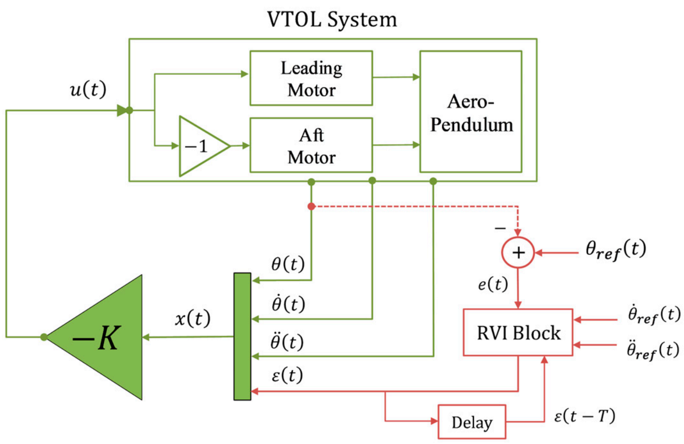

Figure 6. The LQ-RVI tracking controller's block diagram. Red lines indicate the add-on to the conventional control scheme to highlight the novelty of the present work.

4. Parameter-Tuning Procedure

The performance of the baseline LQI controller relies on the system's state variations as well as the control input adjustments. The optimal control effort is ensured by assigning appropriate coefficients to the control-weighting matrix and state-weighting matrix, expressed in Equation (38), while solving the optimal control problem.

$$\boldsymbol{Q} = \mathrm{diag}(q_\theta \quad q_{\dot\theta} \quad q_{\ddot\theta} \quad q_\varepsilon), \boldsymbol{R} = p \tag{38}$$

However, the heuristic tuning of these matrices is constrained by the designer's expertise, potentially limiting the system's ability to precisely follow reference trajectory and recover optimally from disturbances. Similarly, the performance of the RVI block in the prescribed control scheme, formulated in Equation (37), relies on the predefined settings of the following set of control parameters.

$$K_a,\ \alpha_{\max}, \text{ and } \delta_{\max} \tag{39}$$

The cost function given in Equation (40) is minimized to optimize the controller parameters offline.

$$J_e = \int_0^t (e(\tau)^2 + u(\tau)^2)\, d\tau \tag{40}$$

The cost function assigns equal weightage to both variables to effectively minimize the error while concurrently economizing the control energy expenditure to achieve this objective. The weights for the state and control costs, q_x and p, are tuned within a range of 0 to 100. Keeping in view the influence of K_a, $\alpha_{\max}$, and $\delta_{\max}$ on the control law, their values are selected from the range 0 and 10.

An overview of the parameter optimization procedure is depicted in Figure 7 [1]. Section 5 details the experimental procedure used for tuning these parameters. The optimization process begins with the initial settings of $\boldsymbol{Q} = \mathrm{diag}(1 \quad 1 \quad 1 \quad 1)$, $\boldsymbol{R} = 0.1$, $K_a = 1$, $\alpha_{\max} = 1$, and $\delta_{\max} = 0.1$. Each trial involves appropriately adjusting the parameters, allowing the aero-pendulum to track and stabilize itself at a reference setpoint of +60 deg. (counterclockwise) from its rest position and maintaining its balance for 40 s to measure the cost function $J_{e,k}$, where k denotes the trial number. The algorithm searches the entire parameter space by following the descending gradient of the prescribed cost function [17]. If the current cost $J_{e,k}$ is lower than that of the previous trial $J_{e,k-1}$, the global minimum cost variable $J_{e,\min}$ is updated accordingly. The search for the optimal solution concludes either when the maximum number of trials $k_{\max}$ is reached or when $J_{e,\min}$ converges to a predefined threshold. The threshold value is determined heuristically via preliminary algorithmic runs.

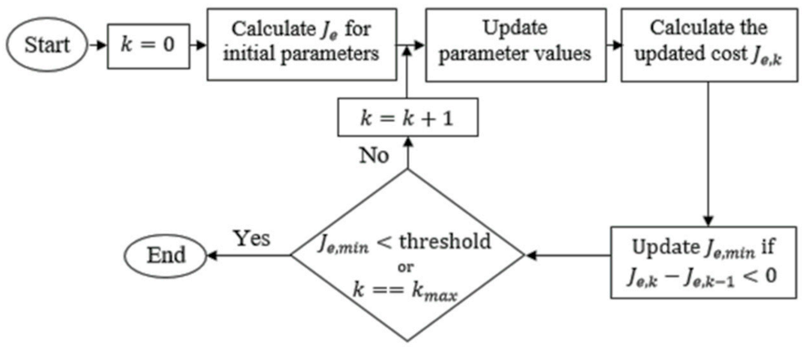

Figure 7. Flow of the parameter-tuning process [17].

These pilot tests help identify a threshold that balances computational efficiency with solution quality, preventing both unnecessary processing and premature termination of the tuning process. For the initial settings of $\boldsymbol{Q}$, $\boldsymbol{R}$, K_a, $\alpha_{\max}$, and $\delta_{\max}$, the minimum recorded cost is $J^0_{e,\min} \approx 0.62 \times 10^6$. Typically, a fraction of $J^0_{e,\min}$ is selected as the stopping criterion to ensure the algorithm converges efficiently without excessive computation. A higher scale value increases the computational load, while a lower value may cause the process to end too early. Hence, the algorithm is terminated when either $J_{e,\min} \rightarrow$

$0.01\, J_{e,\min}^{0}$ or $k_{\max}$ condition is met. Hence, in this study, the threshold for $J_{e,\min}$ is set to 0.6×10^{4} and $k_{\max}$ is set to 25.

The parameter settings thus evaluated for the controllers designed in this study are $\boldsymbol{Q} = \mathrm{diag}(65.82 \quad 8.66 \quad 2.15 \quad 50.74)$, $\boldsymbol{R} = 1.14$, and $K_a = 8.18$, $\alpha_{\max} = 36.8$, and $\delta_{\max} = 25.6$. The corresponding state feedback gains, calculated using Equation (18), are $\boldsymbol{K} = [-9.57 \quad -3.26 \quad -1.08 \quad 11.24]$.

5. Experimental Evaluation

The specific hardware setup and the scenarios for experimentally characterizing the performance of the prescribed control scheme are detailed in this section. The performance of the LQ-RVI tracking controller is benchmarked against the baseline LQI tracking controller via customized hardware-in-the-loop experiments.

5.1. Experimental Setup

The aero-pendulum's platform used for hardware-in-the-loop (HIL) experimentation is displayed in Figure 8. Two +12.0 V DC motors with propellers, having a diameter of 0.20 m, are connected coaxially at the free end of a lightweight aluminum rod. At the rod's pivot end, a rotary encoder is connected. The encoder measures the rod's angular displacement $\theta(t)$ in real-time and feeds the acquired data to an 8-bit embedded microcontroller (Arduino Uno by Sparkfun Electronics). The said microcontroller serves as a serial communication relay between the hardware platform and the software control procedure. The digitized encoder measurements are serially transmitted at 9600 bps to a customized control application that is implemented using the MATLAB/Simulink 2018b. The software is operated on a 64-bit and 1.8 GHz personal computer with 8.0 GB RAM. The sampling frequency is set at 500 Hz. The microcontroller is interfaced with Simulink 2018b by installing the support packages for the Arduino Uno hardware. The control application receives the updated values of $\theta(t)$ after sampling instant and evaluates its higher order derivates, $\dot{\theta}(t)$ and $\ddot{\theta}(t)$, using the built-in numerical differentiation blocks. Once all state variables are acquired, the updated control signals are computed. Apart from the control computations, the aforementioned software application also helps graphically visualize real-time state variations during HIL experiments. It also logs the data for analysis. The control procedure modifies the control signals and serially transmits them to the microcontroller.

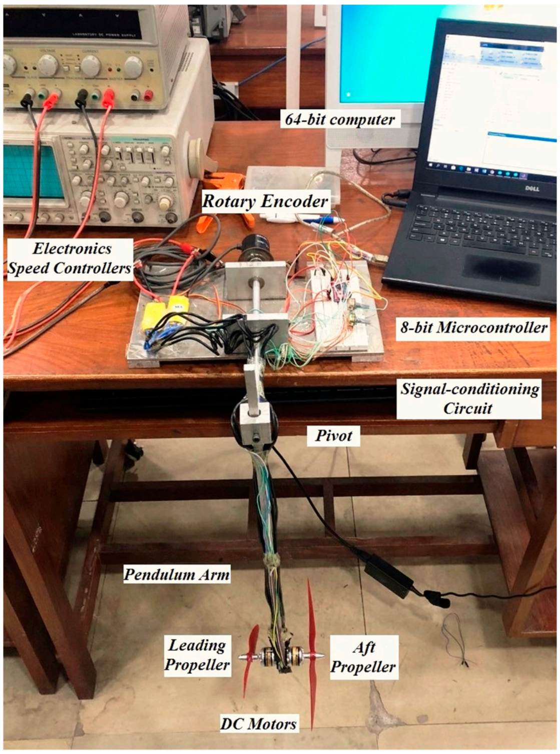

Figure 8. The aero-pendulum setup for VTOL UAV experiments.

The microcontroller converts the acquired data into corresponding PWM signals. It applies them to the electronic speed controller (ESC) of each brushless DC motor to vary the thrust generated by the propellers. For reference, the pitch angle of the aero-pendulum is regarded as zero degrees when it is at rest or suspended freely. The control signal $u(t)$ is bounded between ± 12.0 V to avoid actuator saturation.

5.2. Tests and Results

The control behavior of the closed-loop aero-pendulum system for VTOL applications is evaluated using the following five test cases. These customized test cases provide insights into the robustness, disturbance handling, and tracking ability of the proposed LQ-RVI controller, benchmarked against the LQI controller, under different real-world conditions.

A. Step reference tracking: A VTOL drone typically encounters step changes in pitch (or thrust) when it is required to perform precise maneuvers, such as takeoff, landing, or hovering at a new position. Hence, this test case evaluates the system's capability to track sudden changes in the reference input. The test is conducted by applying a reference input of +60 deg. (counterclockwise) to a resting aero-pendulum, as shown in Figure 9. The reference-tracking ability of the two controllers is depicted in Figure 10.

B. Modeling-error compensation: A VTOL drone typically experiences uncertainties due to unmodeled dynamics, parameter variations (e.g., changing mass during flight), or aerodynamic nonlinearities. Hence, this test assesses the controller's robustness when there are inaccuracies or real-time variations in the system model. To perform the test, a mass of 0.15 kg is added with the pendulum's arm at t = 0 sec. mark, as shown in Figure 11. This modification alters the system's dynamics and hence the coefficients of the matrix $\boldsymbol{A}$, which eventually dampens the system's time domain profile. The subsequent behavior of each controller is depicted in Figure 12.

C. Noise compensation: A VTOL drone relies on sensors to estimate state variables. However, these sensors are prone to noise, especially in turbulent environments. Hence, this test case evaluates the controller's immunity against measurement noise from sensors. The test is performed by introducing a band-limited white-noise signal, having a frequency of 1.0 Hz and a signal-to-noise ratio of 20 dB, as a random sequence in the error signal $e(t)$. The consequent time domain profiles displayed by each controller are illustrated in Figure 13.

D. Impulsive-disturbance rejection: During flight, a VTOL drone often encounters impulsive disturbances contributed by gusts of wind, bird strikes, or mechanical shocks. Hence, this test case evaluates the system's ability to reject abrupt (impulse-like) external forces. The test is conducted by injecting a pulse signal, having a magnitude of ±1.0 V and duration of 100.0 ms, in the system's control input. The positive pulse is injected at t = 20 s. and the negative pulse is injected at t = 40 s. The disruptions in the time domain profiles of each controller are illustrated in Figure 14.

E. Payload-imbalance compensation: A VTOL drone often operates in environments with steady external forces, such as constant wind drift or step variations caused by payload imbalance. Thus, this test case measures the system's ability to compensate for such continuous external forces or disturbances. The test is performed by suddenly adding the 0.15 kg mass beneath the pendulum's arm, as shown in Figure 8, at t = 30 sec. mark. The perturbations in the time domain profiles of each controller are illustrated in Figure 15.

F. Multi-step reference tracking: To execute flight missions involving precise maneuvers, a VTOL drone is required to follow a sequence of target angular positions over time. Thus, this test case measures the system's robustness to track step variations in the reference trajectory. The test is conducted by applying a reference input of +60 deg. (counterclockwise) to a resting aero-pendulum, followed by a step change of +30 deg. (counterclockwise). The multi-step reference tracking ability of each controller is depicted in Figure 16.

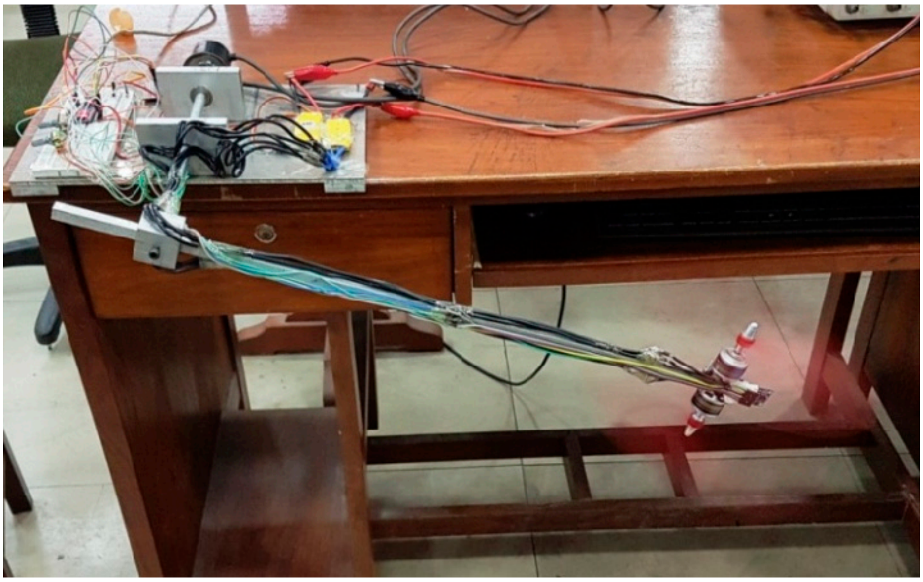

Figure 9. Pendulum at an angular position of 60.0 deg.

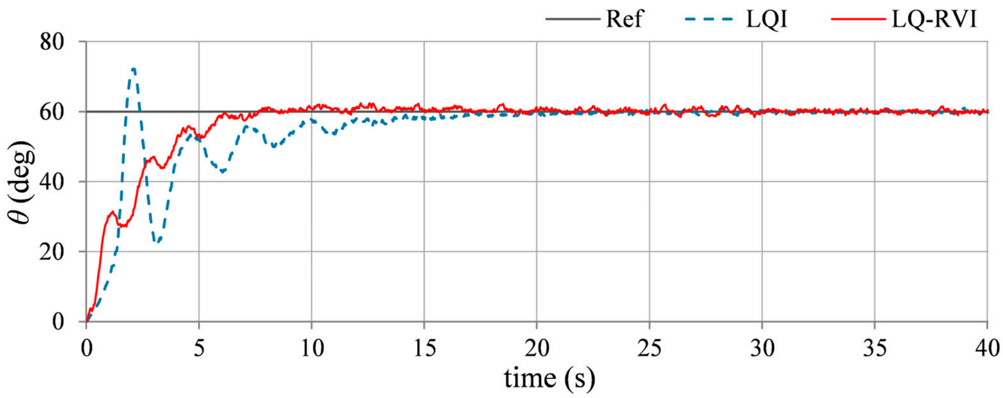

Figure 10. Aero-pendulum's step reference tracking response under nominal conditions.

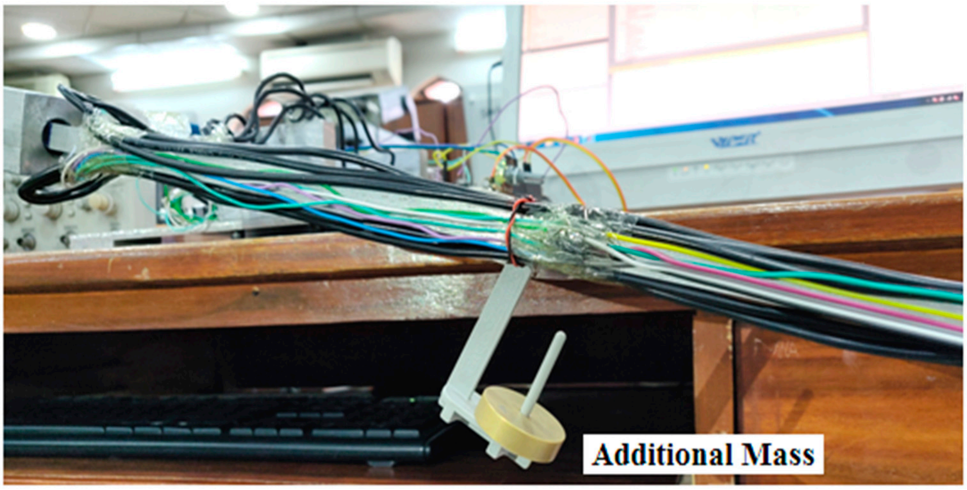

Figure 11. Aero-pendulum setup with additional mass attached beneath its arm [6].

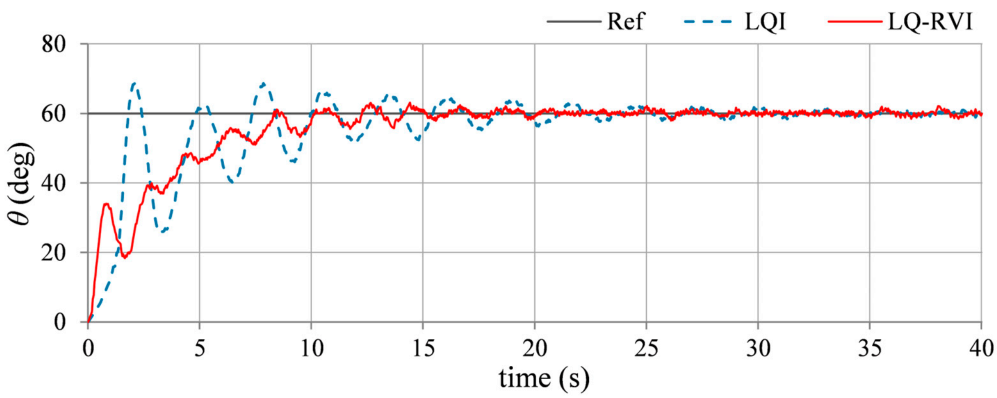

Figure 12. Aero-pendulum's step reference-tracking response under model variations.

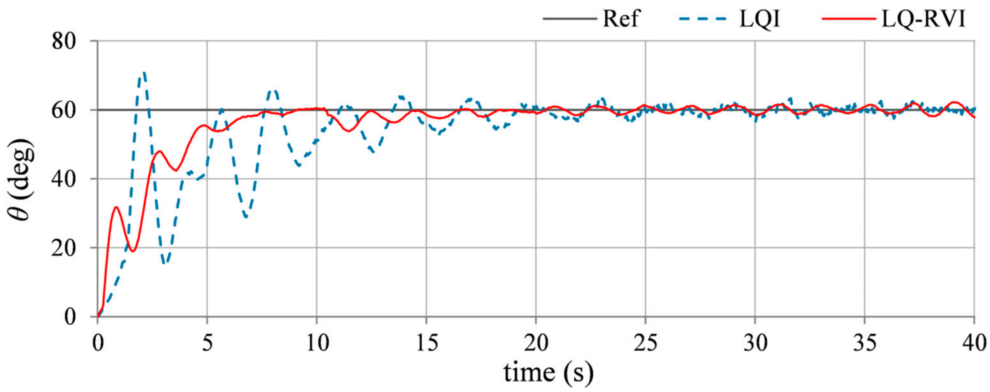

Figure 13. Aero-pendulum's step reference-tracking response under white noise.

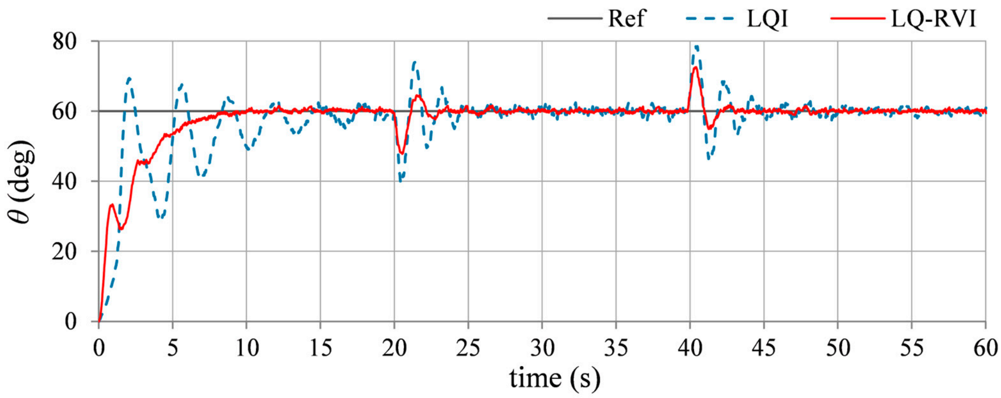

Figure 14. Aero-pendulum's step reference-tracking response under impulsive disturbances.

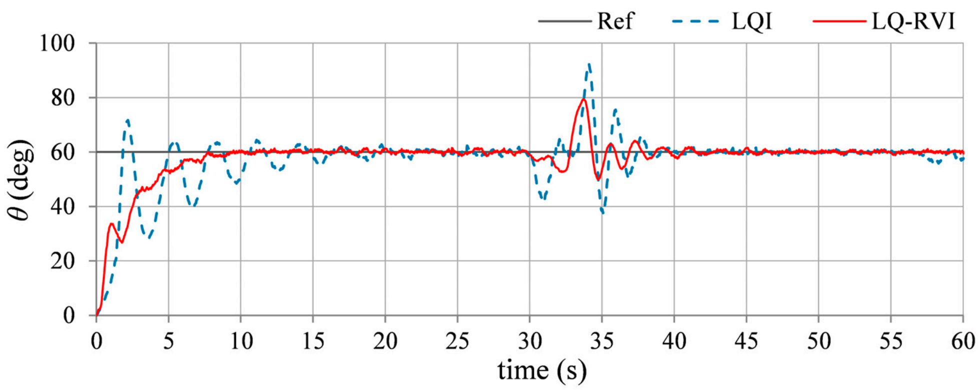

Figure 15. Aero-pendulum's step reference-tracking response under sudden payload imbalance.

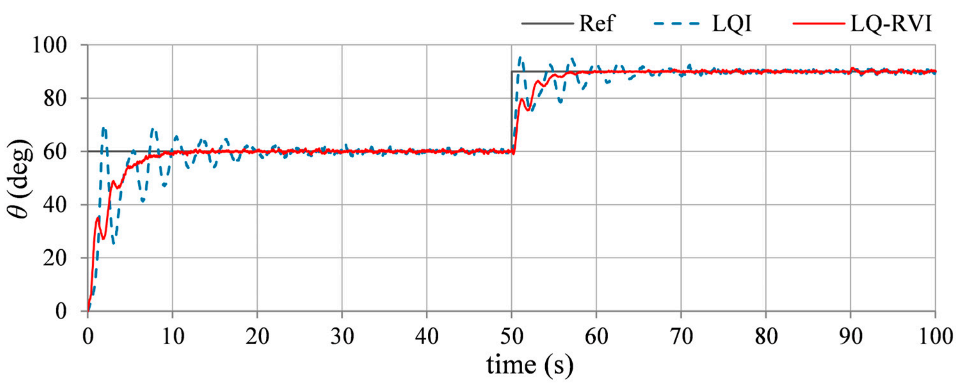

Figure 16. Aero-pendulum's multi-step reference-tracking response under nominal conditions.

5.3. Discussions

The experimental results are analyzed via the following performance indices:

- E_{ss}: The root mean squared value of error $e(t)$. It is computed as $\sum\sqrt{\frac{(e(n))^2}{n}}$, where n is the total number of samples;
- t_s: Time taken by the response to settle within ±2% of the reference value;
- t_{rec}: Time taken by the response to recover and settle within ±2% of the reference value following a disturbance;
- OS: Magnitude of the peak overshoot of response during the initial start-up;
- M_p: Magnitude of the peak overshoot or undershoot of response after a disturbance;
- U_{ms}: The mean-squared value of the control input voltage, providing an estimate of the average control energy consumed by the controller.

Table 2 summarizes the experimental results. The outcomes validate the proposed control law's robust tracking and disturbance rejection capacity.

In Test A and Test F (Figures 10 and 16), the LQI controller exhibits mediocre tracking of the reference step input, with a noticeable overshoot followed by oscillations and a longer settling time. The LQ-RVI shows a relatively better tracking ability, negligible overshoot, faster convergence rate, minimal steady-state fluctuations, and an improved control input economy. In Test B (Figure 12), the LQI maintains an oscillatory tracking performance while exhibiting sensitivity to changes in the model parameter, with a slight degradation in accuracy and settling time. The LQ-RVI controller manifests relatively better robustness and enhanced adaptability to model uncertainties while minimizing the control energy expenditure.

Table 2. Summary of experimental results where A-F denote the tests referred in the description

Experiment	Performance Index		Tracking Controller		Improvement (%)
	Symbol	Unit	LQI	LQ-RVI	
A	E_{ss}	deg.	10.78	8.85	17.9
	OS	deg.	12.16	2.02	83.4
	t_s	sec.	15.52	5.96	61.6
	U_{ms}	V^2	21.41	19.96	6.8
B	E_{ss}	deg.	10.97	9.59	12.6
	OS	deg.	8.98	1.57	82.5
	t_s	sec.	18.75	9.82	47.6
	U_{ms}	V^2	22.71	21.48	5.4
C	E_{ss}	deg.	11.07	8.26	25.4
	OS	deg.	11.08	0.48	95.7
	t_s	sec.	17.15	7.64	55.5
	U_{ms}	V^2	23.26	22.19	4.6
D	E_{ss}	deg.	10.18	7.75	23.9
	M_p	deg.	22.29	12.54	43.7
	t_{rec}	sec.	4.41	2.83	35.8
	U_{ms}	V^2	24.66	23.25	5.7
E	E_{ss}	deg.	10.79	8.48	21.4
	M_p	deg.	32.58	19.44	40.33
	t_{rec}	sec.	8.92	7.33	17.8
	U_{ms}	V^2	23.74	22.06	7.1
F	E_{ss}	deg.	14.28	12.35	13.5
	OS	deg.	10.09	0.17	98.3
	t_s	sec.	15.28	5.54	63.7
	U_{ms}	V^2	25.56	24.08	5.8

In Test C (Figure 13), the LQI controller exhibits poor noise rejection behavior with consistent perturbations in the response. The LQ-RVI controller improves the noise rejection behavior, exhibiting a smoother response under the same noise-disturbance levels. In Test D (Figure 14), the LQI-controlled system experiences noticeable deviations from the reference trajectory, followed by a slower recovery. The LQ-RVI controller effectively dampens the impulsive disturbances and quickly reverts the response to the reference position while effectively attenuating the peak control input requirements. The response highlights the controller's enhanced resilience to abrupt disturbances. In Test E (Figure 15), the LQI controller struggles to maintain steady-state accuracy after the introduction of the disturbance(s). It also demonstrates a relatively slower transient recovery response. The LQ-RVI controller exhibits a comparatively better trajectory-tracking accuracy by efficiently reacting to the payload variations.

The LQI controller exhibits a conservative tracking capability and lacks robustness against disturbances and model uncertainties in every testing scenario. In contrast, the LQ-RVI controller offers precise tracking behavior and superior robustness across all scenarios, including noise, disturbances, and model variations. The enhanced performance of the LQ-RVI controller is credited to the augmentation of the rate-varying integrator with the baseline LQI controller, which speeds up the response and attenuates the overshoots as well as the consequent oscillations during the start-up phase, the disturbance conditions, and the braking phase. The intuitive and self-learning capability of the proposed controller enables it to handle the parametric uncertainties efficiently.

5.4. Sensitivity Analysis

The parameters K_{a}, $\alpha_{\max}$, and $\delta_{\max}$ directly impact the controller's adaptability, responsiveness, and robustness against nonlinearities. As discussed in Section 3, the parameter K_{a} regulates the magnitude of the braking force applied by the braking acceleration compensator (BAC) on the control law. The parameter $\alpha_{\max}$ regulates the responsiveness of the velocity-driven integral modulator (VDIM) to variations in velocity error. Finally, the parameter $\delta_{\max}$ modulates the dynamic sensitivity of the BAC, ensuring smooth modulation of the braking effort.

To evaluate the efficacy of these parameter settings and their influence on the LQ-RVI controller's behavior, a detailed sensitivity analysis was conducted by subjecting the tuned values of K_{a}, $\alpha_{\max}$, and $\delta_{\max}$, as specified in Section 4, to a 10.0% decrease and a 10.0% increase, separately. Experiment A is conducted to assess the system's reference tracking behavior under nominal conditions for each modified parameter configuration. The time-domain reference-tracking profiles of the LQ-RVI controlled system for three different settings of each parameter (K_{a}, $\alpha_{\max}$, and $\delta_{\max}$) are shown separately in Figures 17–19, respectively. Table 3 presents a quantitative overview of the sensitivity analysis.

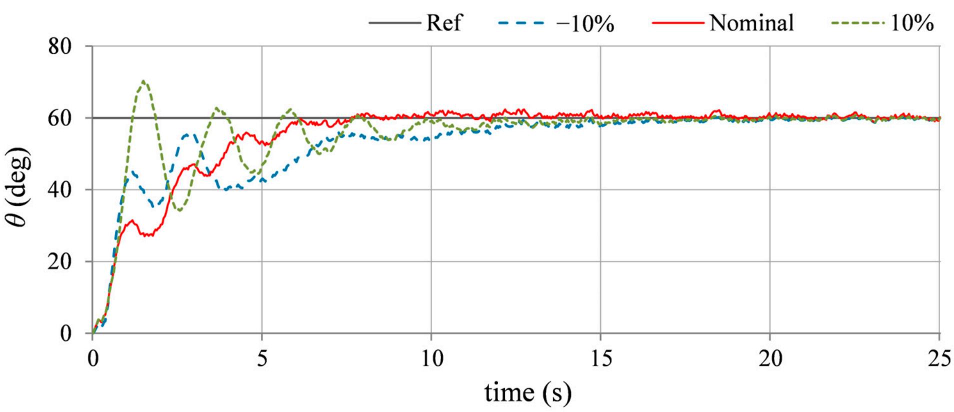

Figure 17. Aero-pendulum's reference tracking response under different settings of K_{a}.

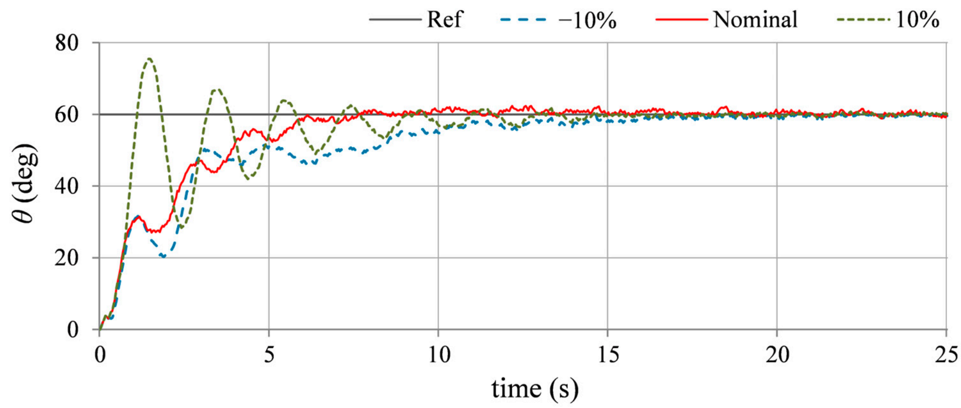

Figure 18. Aero-pendulum's reference tracking response under different settings of $\alpha_{\max}$.

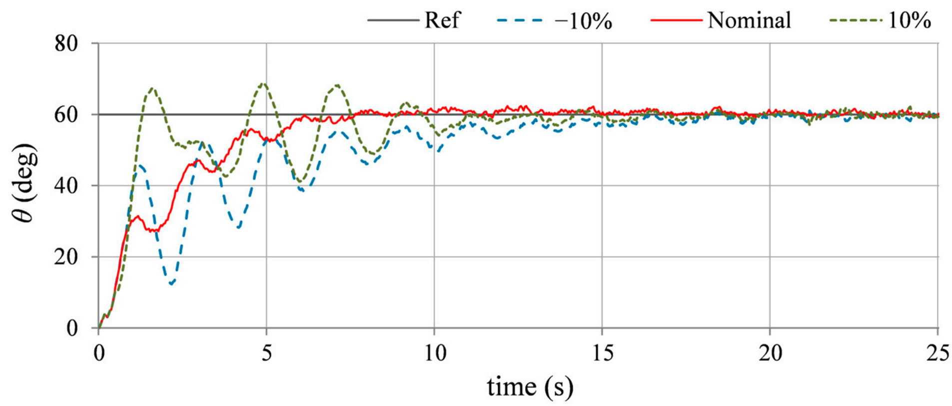

Figure 19. Aero-pendulum's reference tracking response under different settings of $\delta_{\max}$.

Table 3. Quantitative sensitivity analysis of the LQ-RVI controller.

Parameter	Performance Index		Parameter Setting		
	Symbol	Unit	+10% Change	Nominal	−10% Change
K_a	E_{ss}	deg.	8.17	8.85	9.87
	OS	deg.	10.27	2.02	1.01
	t_s	sec.	8.72	5.96	11.05
	U_{ms}	V^2	22.05	19.96	18.84
$\alpha_{\max}$	E_{ss}	deg.	8.25	8.85	10.09
	OS	deg.	15.47	2.02	1.39
	t_s	sec.	7.85	5.96	11.14
	U_{ms}	V^2	21.92	19.96	18.92
$\delta_{\max}$	E_{ss}	deg.	8.11	8.85	10.83
	OS	deg.	9.01	2.02	1.87
	t_s	sec.	9.66	5.96	12.52
	U_{ms}	V^2	22.38	19.96	19.13

The findings of the sensitivity analysis confirm that the nominal parameter settings produce the best tracking accuracy while maintaining a reasonable settling time. A large value of K_a slightly enhances the compensator's response speed during the deceleration phase, but it also introduces large persistent oscillations in the response, and vice versa. A large value of $\alpha_{\max}$ makes the system more responsive to abrupt velocity changes, improving tracking accuracy. However, it also leads to highly disruptive control action, inevitably introducing chattering in the response. A large value of $\delta_{\max}$ improves the compensator's responsiveness during large error conditions (such as initial start-up or disturbances). However, this improved sensitivity also introduces (decaying) oscillations in the response, and vice versa.

6. Conclusions

This study demonstrates the effectiveness of an optimal LQI tracking controller augmented with a nonlinear adaptive integral compensator for precise and robust positioning of VTOL UAVs equipped with contra-rotating propellers. The proposed LQ-RVI controller, built upon a baseline LQI tracker framework, accurately tracks the reference trajectory while effectively rejecting the bounded exogenous disturbances. The integration of a rate-varying nonlinear scaling function, as well as the inclusion of braking acceleration with the baseline LQI controller, significantly enhances the system's tracking accuracy, reduces overshoot, improves transient response, and minimizes control energy consumption, as evidenced by hardware-in-the-loop experiments on an aero-pendulum testbed. These results highlight the proposed LQ-RVI controller's robustness and practical viability for UAV and drone applications operating under external disturbances. Future research can explore the application of the proposed controller to fully-actuated VTOL UAVs in three-dimensional flight scenarios. Investigating its integration with adaptive and machine learning-based frameworks could further enhance its robustness and adaptability to varying operational conditions. Additionally, experimental validation on actual UAV platforms and its scalability to swarm coordination and autonomous navigation tasks under real-world uncertainties represent promising avenues for extending this research.

Author Contributions: Conceptualization, O.S.; methodology, O.S.; software, O.S. and M.K.; validation, J.I.; formal analysis, O.S.; investigation, M.K.; resources, J.I.; data curation, M.K.; writing—original draft preparation, O.S.; writing—review and editing, J.I.; visualization, M.K.; supervision, J.I.; project administration, J.I. All authors have read and agreed to the published version of the manuscript.

Funding: This research received no external funding.

Data Availability Statement: The data presented in this study are available on request from the corresponding author.

Conflicts of Interest: The authors declare no conflicts of interest.

References

1. Ducard, G.; Carughi, G. Neural Network Design and Training for Longitudinal Flight Control of a Tilt-Rotor Hybrid Vertical Takeoff and Landing Unmanned Aerial Vehicle. *Drones* **2024**, *8*, 727.
2. Ducard, G.J.; Allenspach, M. Review of designs and flight control techniques of hybrid and convertible VTOL UAVs. *Aerosp. Sci. Technol.* **2021**, *118*, 107035.
3. Elmeseiry, N.; Alshaer, N.; Ismail, T. A detailed survey and future directions of unmanned aerial vehicles (uavs) with potential applications. *Aerospace* **2021**, *8*, 363.
4. Ozdemir, U.; Aktas, Y.O.; Vuruskan, A.; Dereli, Y.; Tarhan, A.F.; Demirbag, K.; Inalhan, G. Design of a commercial hybrid VTOL UAV system. *J. Intell. Robot. Syst.* **2014**, *74*, 371–393.
5. Enikov, E.T.; Campa, G. Mechatronic aeropendulum: Demonstration of linear and nonlinear feedback control principles with matlab/simulink real-time windows target. *IEEE Trans. Educ.* **2012**, *55*, 538–545.
6. Saleem, O.; Rizwan, M.; Zeb, A.A.; Ali, A.H.; Saleem, M.A. Online adaptive PID tracking control of an aero-pendulum using PSO-scaled fuzzy gain adjustment mechanism. *Soft Comput.* **2020**, *24*, 10629–10643.
7. Rojas-Galván, R.; García-Martínez, J.R.; Cruz-Miguel, E.E.; Barra-Vázquez, O.A.; Olmedo-García, L.F.; Rodríguez-Reséndiz, J. Hunting Search Algorithm-Based Adaptive Fuzzy Tracking Controller for an Aero-Pendulum. *Technologies* **2024**, *12*, 63.
8. Panjwani, B.; Quinsard, C.; Przemysław, D.G.; Furseth, J. Virtual Modelling and Testing of the Single and Contra-Rotating Co-Axial Propeller. *Drones* **2020**, *4*, 42.

9. Filippone, A. Historical development of the coaxial contra-rotating propeller. *The Aeronaut. J.* **2023**, *127*, 699–736.
10. Xu, J.; Yu, J.; Lu, X.; Long, Z.; Xu, Y.; Sun, H. Aerodynamic Performance and Numerical Analysis of the Coaxial Contra-Rotating Propeller Lift System in eVTOL Vehicles. *Mathematics* **2024**, *12*, 1056.
11. Roberts, A.; Tayebi, A. Adaptive Position Tracking of VTOL UAVs. *IEEE Trans. Robot.* **2011**, *27*, 129–142.
12. Deng, B.; Xu, J.; Yuan, X.; Yu, S. Active Disturbance Rejection Flight Control and Simulation of Unmanned Quad Tilt Rotor eVTOL Based on Adaptive Neural Network. *Drones* **2024**, *8*, 560.
13. Su, J.; Huang, H.; Zhang, H.; Wang, Y.; Wang, F.Y. eVTOL Performance Analysis: A Review From Control Perspectives. *IEEE Trans. Intell. Veh.* **2024**, *9*, 4877–4889.
14. Tutsoy, O.; Hendoustani, D.; Ahmadi, K.; Nabavi, Y.; Iqbal, J. Minimum distance and minimum time optimal path planning with bioinspired machine learning algorithms for impaired unmanned air vehicles. *IEEE Trans. Intell. Transp. Syst.* **2024**, *25*, 9069–9077.
15. Tassanbi, A.; Ali Khan, A.; Kashkynbayev, A.; Shehab, E.; Duc Do, T.; Ali, M.H. Performance evaluation of developed controllers for unmanned aerial vehicles with reference camera. *Meas. Control* **2024**, 00202940241270863, https://doi.org/10.1177/00202940241270863.
16. Rosmadi, N.H.B.; Bingi, K.; Devan, P.A.M.; Korah, R.; Kumar, G.; Prusty, B.R.; Omar, M. Fractional-Order Control Algorithm for Tello EDU Quadrotor Drone Safe Landing during Disturbance on Propeller. *Drones* **2024**, *8*, 566.
17. Saleem, O.; Iqbal, J. Phase-Based Adaptive Fractional LQR for Inverted-Pendulum-Type Robots: Formulation and Verification. *IEEE Access* **2024**, *12*, 93185–93196.
18. Liu, X.; Xu, J.; Liu, Y. Trajectory tracking and point stability of three-axis aero-dynamic pendulum with MPC strategy in disturbance environment. *Assem. Autom.* **2021**, *41*, 358–368.
19. Gong, B.; Li, Y.; Zhang, L.; Ai, J. Adaptive Factor Fuzzy Controller for Keeping Multi-UAV Formation While Avoiding Dynamic Obstacles. *Drones* **2024**, *8*, 344.
20. Ren, R.; Wang, Z.; Ma, H.; Ji, B.; Tao, F. High-Order Disturbance Observer-Based Fuzzy Fixed-Time Safe Tracking Control for Uncertain Unmanned Helicopter with Partial State Constraints and Multisource Disturbances. *Drones* **2024**, *8*, 679.
21. Bacha, A.; Chelihi, A.; Glida, H.E.; Sentouh, C. Fixed-Time Fault-Tolerant Adaptive Neural Network Control for a Twin-Rotor UAV System with Sensor Faults and Disturbances. *Drones* **2024**, *8*, 467.
22. Rafiuddin, N.; Khan, Y.U. Nonlinear controller design for mechatronic aeropendulum. *Int. J. Dyn. Control* **2023**, *11*, 1662–1670.
23. Yan, Y.; Cao, H.; Zhang, B.; Ni, W.; Wang, B.; Ma, X. Large-Scale Solar-Powered UAV Attitude Control Using Deep Reinforcement Learning in Hardware-in-Loop Verification. *Drones* **2024**, *8*, 428.
24. Irfan, S.; Zhao, L.; Ullah, S.; Javaid, U.; Iqbal, J. Differentiator- and Observer-Based Feedback Linearized Advanced Nonlinear Control Strategies for an Unmanned Aerial Vehicle System. *Drones* **2024**, *8*, 527.
25. Habib, G.; Miklos, A.; Enikov, E.T.; Stepan, G.; Rega, G. Nonlinear model-based parameter estimation and stability analysis of an aero-pendulum subject to digital delayed control. *Int. J. Dyn. Control* **2017**, *5*, 629–643.
26. Feng, Y.; Hu, Q.; Wu, W.; Wu, L.; Guo, Q.; Zhang, H. A Nonlinear Adaptive Control and Robustness Analysis for Autonomous Landing of UAVs. *Drones* **2024**, *8*, 587.
27. Breganon, R.; Alves, U.N.L.; de Almeida, J.P.L.; Ribeiro, F.S.; Mendonça, M.; Palácios, R.H.; Montezuma, M.A. Model identification and $H\infty$ control of an aeropendulum. *J. Appl. Res. Technol.* **2023**, *21*, 526–534.
28. Shen, Y.; Chen, M. Robust backstepping control for maneuver aircraft based on event-triggered mechanism and nonlinear disturbance observer. *Aircr. Eng. Aerosp. Technol.* **2023**, *95*, 1016–1028.
29. Hassani, H.; Mansouri, A.; Ahaitouf, A. Backstepping-based supertwisting sliding mode attitude control for a quadrotor aircraft subjected to wind disturbances: Experimental validation. *Int. J. Dyn. Control* **2023**, *11*, 1285–1296.
30. Kuang, J.; Chen, M. Adaptive Sliding Mode Control for Trajectory Tracking of Quadrotor Unmanned Aerial Vehicles Under Input Saturation and Disturbances. *Drones* **2024**, *8*, 614.
31. Saleem, O.; Rizwan, M.; Iqbal, J. Adaptive optimal control of under-actuated robotic systems using a self-regulating nonlinear weight-adjustment scheme: Formulation and experimental verification. *PLoS ONE* **2023**, *18*, e0295153.
32. Saleem, O.; Iqbal, J. Fuzzy-immune-regulated adaptive degree-of-stability LQR for a self-balancing robotic mechanism: Design and HIL realization. *IEEE Rob. Autom. Lett.* **2023**, *8*, 4577–4584.
33. Madeiras, J.; Cardeira, C.; Oliveira, P.; Batista, P.; Silvestre, C. Saturated Trajectory Tracking Controller in the Body-Frame for Quadrotors. *Drones* **2024**, *8*, 163.
34. Whidborne, J.F.; Mendez, A.P.; Cooke, A. Effect of Rotor Tilt on the Gust Rejection Properties of Multirotor Aircraft. *Drones* **2022**, *6*, 305.

35. Chwa, D. Fuzzy adaptive output feedback tracking control of VTOL aircraft with uncertain input coupling and input-dependent disturbances. *IEEE Trans. Fuzzy Syst.* **2014**, *23*, 1505–1518.
36. Su, S.; Lin, Y. Output tracking control for a velocity-sensorless VTOL aircraft with measurement delays. *Int. J. Syst. Sci.* **2015**, *46*, 885–895.
37. Yan, S.; Gu, Z.; Park, J.H.; Xie, X. A delay-kernel-dependent approach to saturated control of linear systems with mixed delays. *Automatica* **2023**, *152*, 110984.
38. Yan, S.; Gu, Z.; Park, J.H.; Xie, X. Distributed-Delay-Dependent Stabilization for Networked Interval Type-2 Fuzzy Systems with Stochastic Delay and Actuator Saturation. *IEEE Trans. Syst. Man. Cybern. Syst.* **2023**, *53*, 3165–3175.
39. Yang, S.F.; Chou, J.H. A mechatronic positioning system actuated using a micro DC-motor-driven propeller–thruster. *Mechatronics* **2009**, *19*, 912–926.
40. Murk Junejo, Arbab Nighat Kalhoro, Arsha Kumari, Fuzzy Logic Based PID Auto Tuning Method of QNET 2.0 VTOL, I.J. Information Technology and Computer Science, 2020, 1, 9-16, DOI: 10.5815/ijitcs.2020.01.02.
41. Ilyas, M.; Aziz, S.; Shah, I.; Khan, A.; Jung, D.W. Experimental Stability Analysis of Vertical Takeoff and Landing System Based on Robust Control Strategy. *Appl. Sci.* **2023**, *13*, 11209.
42. Aguas, X.; Revelo, J.; Paredes, I.; Cuaycal, A.; Herrera, M. Integral-optimal sliding mode control for vertical take-off and landing system. In Proceedings of the 2018 International Conference on Information Systems and Computer Science, Quito, Equador, 13–15 November 2018; pp. 29–35.
43. Saleem, O.; Iqbal, J.; Afzal, M.S. A robust variable-structure LQI controller for under-actuated systems via flexible online adaptation of performance-index weights. *PLoS ONE* **2023**, *18*, e0283079.
44. Lewis, F.L.; Vrabie, D.; Syrmos, V.L. *Optimal Control*, 3rd ed.; John Wiley & Sons: Hoboken, NJ, USA, 2012.
45. Reza Sabaapour, M.; Khanmirza, E.; Ghadami, S. An anti-windup rate-varying integral control applied to electromechanical actuator. *J. Mech. Eng. Sci.* **2015**, *229*, 692–702.